ACS Catalysis

Research Article

pubs.acs.org/acscatalysis

Total Oxidation of Formaldehyde over MnO_x-CeO_2 Catalysts: The Effect of Acid Treatment

Jhon Quiroz,[†] Jean-Marc Giraudon,[†] Antonella Gervasini,[‡] Christophe Dujardin,[†] Christine Lancelot,[†] Martine Trentesaux,[†] and Jean-François Lamonier*,[†]

[†]Université Lille1, Sciences et Technologies, Unité de Catalyse et Chimie du Solide UMR CNRS 8181, 59655 Villeneuve d'Ascq Cedex, France

[‡]Università degli Studi di Milano, Dipartimento di Chimica, Via Camillo Golgi 19, I-20133 Milano, Italy

Supporting Information

ABSTRACT: The effect of acid treatment in mixed MnO_x−CeO_2 samples has been investigated in the catalytic total oxidation of formaldehyde. The acid treatment has no effect on the textural and redox properties of the materials when Mn is stabilized in a MnO_x−CeO_2 solid solution (Mn content below 50%). However, these properties were found to be highly altered by acid treatment when the solubility limit of Mn in the ceria was exceeded (Mn content above 50%). This enabled access to the primary porosity and oxidized the manganese species to a higher oxidation state via a Mn dismutation reaction. As a result, the catalytic activity of pure manganese oxide, after chemical activation, in the oxidation of formaldehyde is greatly improved—at 100 °C, the conversion of formaldehyde is increased by a factor of 5 and the corresponding intrinsic reaction rate by 1.4. Combined in situ surface analysis unambiguously identified formate species as a result of formaldehyde oxidation at room temperature on the chemically activated pure MnO_x. The evolution of various surface species was monitored by increasing the temperature and in situ FTIR, and XPS results provided direct evidence of the desorption of monodentate formate species into formaldehyde and the oxidation of bidentate-bridging formate species. Changes in the average oxidation state of surface manganese confirmed the participation of oxygen from MnO_x in the formation of formate species at room temperature and their transformation into CO_2 and H_2O when increasing the temperature.

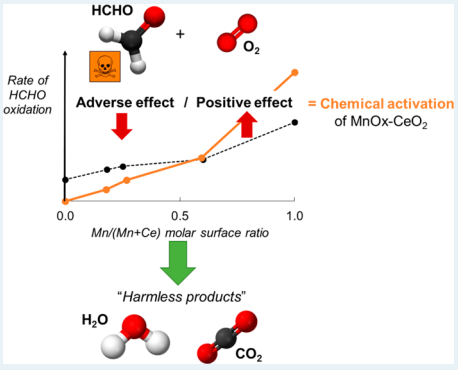

KEYWORDS: *formaldehyde, catalytic oxidation, volatile organic compound (VOC), MnO_x−CeO_2 mixed oxides, chemical activation, indoor pollution*

1. INTRODUCTION

Formaldehyde (HCHO) is a dangerous air pollutant in several indoor environments, including houses, offices, and industrial buildings. Long-term exposure to this pollutant can cause serious health problems,[1] making this a critical molecule to be eliminated to satisfy stringent environmental regulations and improve indoor air quality.[2] Due to the presence of this pollutant in indoor environments, the abatement of HCHO at low temperature has significant practical interest. Among the different strategies that have been proposed to control HCHO emission, heterogeneous catalytic oxidation of HCHO into non harmful CO_2 and H_2O has been highlighted as a promising way to remove formaldehyde with low energy consumption.[3]

Supported noble metals are typically proposed as efficient catalysts to oxidize HCHO at low temperature (<150 °C). For instance, several supported noble-metals catalysts have been developed for low-temperature formaldehyde oxidation, such as Pt/TiO_2,[4,5] Pt/Al_2O_3,[6] Pd/TiO_2,[7,8] Pt/MnO_x-CeO_2,[9] Pt/Fe_2O_3,[10] and Au/Co_3O_4−CeO_2.[11] Among them, the catalyst based on supported Pt exhibits superior catalytic activities at low temperature, and even at room temperature in some cases.[12] However, the replacement of these materials in environmental processes has to be considered, owing to the well-known limitation of the use of these elements (e.g., high price and limited resources).

Bulk and supported transition metal oxides were found to be low-cost promising materials for low-temperature formaldehyde oxidation.[3] For these catalytic systems, the most efficient metal oxides are MnO_x, CeO_2, and Co_3O_4.[11,13,14] In a recent study, improved catalytic activity has been achieved for transition metal oxides with the addition of other metals.[15] Among the transition metal oxides, MnO_x was studied by many research groups, due to its low volatility and low toxicity. Manganese oxides assume a wide range of stoichiometry and crystal phases (β-MnO_2, γ -MnO_2, α-Mn_2O_3, γ -Mn_2O_3, α-Mn_3O_4, and Mn_5O_8) and show excellent catalytic efficiency for HCHO oxidation at low temperature. As two important forms of MnO_x, cryptomelane and birnessite have been investigated in

Received: November 26, 2014
Revised: February 19, 2015
Published: February 19, 2015

DOI: 10.1021/cs501879j
ACS Catal. 2015, 5, 2260−2269

previous reports as suitable catalysts for HCHO oxidation.[16,17] More recently, Averlant et al.[18] showed that one of the most important parameters that influences catalytic activities is the valence state of manganese, and enhanced activities were achieved over materials with high Mn^{4+} content. Consequently, for this application, it is crucial to generate high-valence manganese oxide materials to improve catalytic properties. Brenet et al.[19] studied the chemical activation of manganese oxide in the form of a hausmannite phase (Mn_3O_4) by treatment in acid medium using sulfuric acid. The influence of various factors such as acid concentration and temperature have been specified, and the manganese oxide obtained showed a high Mn oxidation state, enhanced electrochemical properties, and improved catalytic activities. Askar et al.[20] showed that starting from Mn_2O_3 and Mn_3O_4, a higher valence state of manganese was also obtained through the formation of MnO_2 produced by acid digestion. Depending on the type of inorganic acid used, the obtained MnO_2 structure differed: hydrochloric acid (HCl) tended to produce the so-called γ variety while sulfuric acid tended to produce α or γ-MnO_2. The authors explain this result by a proton-assisted rearrangement reaction in the presence of Mn^{2+} ions to change γ-MnO_2 into α-MnO_2. More recently, Sinha et al.[21,22] have synthesized manganese oxide mesoporous materials by using a template-assisted method followed by chemical activation under acid treatment. These materials have a large surface area and enhanced ability to eliminate volatile organic compounds at low temperature. Moreover, addition of ceria was found to further enhance the catalytic activity of MnO_x through the formation of a solid solution, in which the synergistic interaction between manganese and cerium oxides was explained by an oxygen transfer mechanism.[23,24]

In order to obtain materials with high specific surface area and enhanced catalytic activities, a surfactant-assisted wet-chemistry route has been proposed for the preparation of these catalysts. Suib et al.[25] have synthesized manganese oxide with mesoporous structures by oxidation of $Mn(OH)_2$ in the presence of cetyltrimethylammonium bromide (CTAB); the solid obtained showed ordered mesoporous structure and exceptional thermal stability (1000 °C). The synthesis and characterization of high surface area ceria in the presence of a cationic surfactant has also been reported by Trovarelli et al.[26,27] These ceria materials showed enhanced textural properties and thermal resistance compared with those prepared by conventional routes and also improved oxygen storage and redox behavior. However, the ordering of ceria materials was limited to a few regions. More recently, Zou et al.[28] have synthesized MnO_x–CeO_2 by surfactant-assisted precipitation using CTAB as a template; the solids show a high specific surface, and no regular arrangement was observed by TEM, indicating that ordered mesoporous structures were not formed in the solid.

In the present work, calcined mesoporous MnO_x–CeO_2 mixed oxides synthesized by a surfactant-assisted wet-chemistry route are characterized, and the effect of their activation by acid treatment is described. The different solids have been extensively characterized by X-ray diffraction (XRD), nitrogen adsorption–desorption, transmission electron microscopy (TEM), X-ray photoelectron spectroscopy (XPS), and H_2-temperature-programmed reduction (H_2-TPR), in order to highlight the chemical activation and Mn content effects. Their catalytic performances have been evaluated through the complete oxidation of formaldehyde. Concomitantly, HCHO temperature-programmed desorption, in situ XPS, and FTIR studies of a formaldehyde saturated sample have been performed in order to obtain more insight into HCHO reactivity with an activated MnO_x catalyst.

2. EXPERIMENTAL SECTION

2.1. Catalyst Preparation. Binary oxides $(n)MnO_x-(1-n)CeO_2$ (n = 0, 0.25, 0.5, 0.75 and 1) were prepared by coprecipitation of an aqueous solution of Mn and Ce metal nitrates with sodium hydroxide in the presence of cetyltrimethylammonium bromide as a surfactant. In a specific synthesis, stoichiometric quantities of $Mn(NO_3)_2.6H_2O$ (Alfa Aesar 98%) and $Ce(NO_3)_3.6H_2O$ (Alfa Aesar 99%) were dissolved in 150 mL of distilled water followed by the addition of a solution of NaOH (4.8 g NaOH (Sigma-Aldrich ≥98%) in 50 mL of distilled water). The solution containing the resulting manganese–cerium hydroxide precipitate was added to an aqueous solution of cetyltrimethylammonium bromide (CTAB, 67 g (Sigma ≥98%) in 150 mL of distilled water). The resulting mixture was heated to 75 °C and then stirred for 1 h. The final gel obtained in a sealed beaker was transferred to an oven and heated for 12 h at 75 °C. The solid residue was filtered, washed with distilled water, dried in air, and lastly calcined at 500 °C for 6 h (1 °C·min $^{-1}$). A part of the calcined sample was treated with an aqueous solution of H_2SO_4 (120 mL - 10 mol L^{-1}) by stirring in a beaker for 1 h. The final product was filtered, and the residue was washed with water and dried at 105 °C. The samples were labeled by their atomic composition as follows $(n)MnO_x-(1-n)CeO_2$ (n = 0, 0.25, 0.5, 0.75 and 1).

2.2. Catalyst Characterization. X-ray diffraction (XRD) patterns were recorded on a Bruker X-ray diffractometer at room temperature with Cu Kα radiation (λ = 1.5418 Å). The data sets were collected in the 5–80° range with a step size of 0.02° and an integration time of 4 s. The diffraction patterns have been indexed by comparison with the Joint Committee on Powder Diffraction Standards (JCPDS) files.

Nitrogen adsorption/desorption isotherms were obtained at 77K on a Micromeritics ASAP 2010. Before each analysis, the samples were pretreated at 120 °C under vacuum for 3h. The BET and BJH analyses were used to determine the total specific surface area and the pore size distribution of the samples, respectively.

Transmission electronic microscopy (TEM) images were taken on a TECNAI electron microscope operating at an accelerating voltage of 200 kV equipped with a LaB_6 crystal. Prior to TEM observations, samples were deposited from ethanolic solution onto holey-carbon copper grids.

Temperature-programmed reduction by H_2 (H_2-TPR) measurements were performed on a Micromeritics AutoChem apparatus; 50 mg of the sample were heated from room temperature to 800 °C (with a heating rate of 10 °C·min^{-1}) using a mixture of 5% H_2 in argon. These conditions maintained K and P values at around 116 s and 16 °C, respectively,[29] for all the analyses irrespective of the relative amounts of Mn and Ce oxides in the sample.

X-ray photoelectron spectroscopy (XPS) experiments were performed using an AXIS Ultra DLD Kratos spectrometer equipped with a monochromatized aluminum source (Al Kα = 1486.7 eV) and charge compensation gun. All binding energies were referenced to the C 1s core level at 285 eV. Simulation of the experimental photopeaks was carried out using a mixed Gaussian/Lorentzian peak fit procedure according to the

DOI: 10.1021/cs501879j
ACS Catal. 2015, 5, 2260–2269

Table 1. Textural Properties of the Calcined and Acid-Treated Materials

	crystallite size (nm)		BET surface area ($m^2 \cdot g^{-1}$)		maximum pore size diameter (nm)		pore volume ($cm^3 \cdot g^{-1}$)	
sample code (n)	calcined	acid-treated	calcined	acid-treated	calcined	acid-treated	calcined	acid-treated
1	31.0	29.0	20	82	30	5	0.13	0.26
0.75	5.2	4.5	91	160	25	3	0.33	0.43
0.5	5.3	5.1	100	112	30	30	0.23	0.25
0.25	4.8	4.8	130	137	15	15	0.35	0.36
0	10.0	10.0	73	75	15	15	0.23	0.25

software supplied by CasaXPS. Semiquantitative analysis accounted for a nonlinear Shirley background subtraction.

2.3. Catalytic Activity Test. The formaldehyde (HCHO) catalytic oxidation was performed in a fixed bed reactor (i.d. 8−10 mm), loaded with 200 mg of the catalyst sieved between 100 and 270 mesh. The catalyst was activated in situ at 250 °C for 2 h with 20% vol O_2 balanced by He, with a flow rate of 30 mL·min^{-1}. Gaseous formaldehyde was generated from paraformaldehyde (solid) in a permeation tube placed in a permeation chamber (Dynacalibrator, VICI Metronics, Inc.). The permeation device chamber was maintained at a constant temperature of 100 °C. The HCHO was then mixed with the carrier gas O_2/He leading to a gaseous mixture containing 400 ppm of HCHO, 20% vol O_2 balanced by He. The total flow rate was 100 mL·min^{-1}, and the gas hourly space velocity was 30 000 mL·g_{cat}^{-1} h^{-1}. The reactor temperature was increased from 25 to 300 °C (1 °C·min^{-1}). The effluent gas from the reactor was analyzed online using a MicroGC (Varian) chromatograph equipped with a thermal conductivity detector. Separations were carried out using two columns—a 1 m COX column channel for permanent gas analysis and a 8 m CP-Sil 5 CB column channel for the formaldehyde analysis. In the presence of Mn-based catalysts, HCHO was selectively transformed into CO_2 independent of the reaction temperature. The formaldehyde conversion (X_{HCHO}, %) was estimated using the following equation:

$$X_{HCHO}(\%) = \left(1 - \frac{[HCOH]}{[HCOH] + [CO_2]}\right) \times 100$$

[HCHO] and [CO_2] being the concentrations at time t. The carbon balance of the reaction system has been checked to be around 100% for all the conditions and catalysts tested. The average percent error of the analyses was ca. ± 10%, evaluated on repeated measurements.

2.4. Formaldehyde Adsorption and Temperature-Programmed Surface Reaction. The HCHO adsorption and the reactant/products desorption from the catalyst surface were performed in the same apparatus used for the catalytic test. The solid was first pretreated with argon at 150 °C to remove water and surface impurities. A HCHO adsorption curve was obtained at RT to ensure the saturation of the catalyst surface by using mass spectrometry (Omnistar, GSD 301-Pfeiffer). The catalyst was purged with argon for 2 h to remove physically adsorbed HCHO, and then the temperature was increased from RT to 500 °C at a rate of 10 °C·min^{-1} in a continuous flow of argon. The gaseous effluents from the reactor were analyzed by mass spectrometry, HCHO (m/z = 30), CO_2 (m/z = 44), CO (m/z = 28), and H_2O (m/z = 18).

In situ IR studies were carried out with a Nicolet 460 FT-IR spectrometer equipped with a MCT detector. The HCHO saturated sample was pressed into self-supported pellets and was thermally treated from 25 to 420 °C (10 °C·min^{-1}) under a flow of Helium (12 mL·min^{-1}).

In situ XPS analyses were performed using a Vacuum Generators Escalab 220 XL spectrometer equipped with an aluminum source (Al Kα = 1486.6 eV) and a special catalytic cell. The HCHO saturated sample was thermally treated at different temperatures (2 °C·min^{-1}) from 25 to 175 °C under a flow of argon. Once the required temperature was reached, the sample was cooled under Ar to 25 °C, and XPS analysis was then conducted.

3. RESULTS AND DISCUSSION

3.1. Characterization. *3.1.1. Structural, Textural, and Morphologic Characterizations.* The wide-angle powder XRD patterns of the calcined MnO_x−CeO_2 samples are shown in Figure S1a. For low Mn content (n values ranging from 0 to 0.5) samples, all the diffraction peaks can be assigned to a fluorite structure similar to that of pure ceria (JCPDS 34394). No peak related to a manganese oxide phase was observed, probably due to the formation of a Mn−Ce solid solution or the presence of amorphous manganese oxide. The inset in Figure S1a shows that the 2θ for the (220) diffraction peak shifts to higher angles for the (n)MnO_x−(1 − n)CeO_2 samples, with increasing n. This shift can be related to the formation of a MnO_x−CeO_2 solid solution in which manganese ions (Mn^{4+} 0.054 nm, Mn^{3+} 0.066 nm, Mn^{2+} 0.080 nm) replaced Ce^{4+} ions (0.094 nm).[30] Based on the 2θ maximum value of the (220) diffraction peak (Figure S1a inset), the solubility limit of manganese ions into the ceria structure is reached for n = 0.5. Furthermore, the diffraction patterns of high Mn content samples showed the crystallization of a Mn_3O_4 hausmannite phase (JCPDS 071841) together with the fluorite structure (JCPDS 34394). For n = 1, in addition to Mn_3O_4, Mn_2O_3 (JCPDS 070856) and Mn_5O_8 (JCPDS 391218) phases were also detected.

The wide-angle powder XRD patterns of the acid-treated MnO_x−CeO_2 samples are displayed in Figure S1b. After acid treatment, differences were observed only for samples with high Mn content ($n \geq 0.75$): diffraction peaks due to the Mn_3O_4 hausmannite phase disappeared in favor of the unique presence of the Mn_5O_8 monoclinic phase. The Figure S1b inset shows that after the acid treatment the solid solution is retained for $n \leq 0.5$.

Table 1 reveals the crystallite sizes of the calcined and acid-treated samples estimated from the Scherrer equation applied to the (111) (2θ = 28.6°) and (220) (2θ = 47.5°) CeO_2 diffraction peaks and to the (200) (2θ = 22°) Mn_5O_8 diffraction peak for the two cerium free samples. For the calcined samples, the crystallite size was found to be 10 nm for pure ceria, between 4 and 6 nm for the mixed oxides, and around 30 nm for pure manganese oxide. After acid treatment, the crystallite sizes remained unchanged (Table 1).

DOI: 10.1021/cs501879j
ACS Catal. 2015, 5, 2260−2269

The BET surface area values of the pure oxides were much lower than those of the mixed oxides (Table 1). Among the calcined mixed oxides samples, the largest surface area was found to be 130 $m^2 \cdot g^{-1}$ for the $n = 0.25$ sample, and this value is consistent with the lowest crystallite size and the highest pore volume. Interaction between Ce and Mn oxides may produce more open and distorted structures when the two oxides are mixed, resulting in a higher surface area for the binary oxides. The surface area values of the manganese rich samples ($n \geq 0.75$) were greatly increased after the acid treatment (Table 1). After acid treatment, Mn species dismutation can occur according to the following reaction:[19]

$$Mn_3O_4(s) + 4H^+(aq) = MnO_2(s) + 2Mn^{2+}(aq) + 2H_2O(l)$$

However, in this experiment, the metastable Mn_5O_8 phase has been obtained instead of an MnO_2 phase. Thus, a proportion of Mn^{3+} ions in Mn_3O_4 is probably oxidized leading to Mn_5O_8, stabilizing some Mn^{2+} ions inherited from Mn_3O_4. The dissolution of Mn^{2+} ions may occur first from the amorphous phases located between the crystallites, thus revealing a higher surface area (Figure S2). Such a high increase of the surface area was not observed for $n \leq 0.5$ (Table 1). This discrepancy could be explained by the stabilization of Mn ions in the mixed oxide. For ceria, all the data from textural studies are similar (Table 1). This result can be explained by the slow dissolution of CeO_2 in sulfuric acid.[31]

Figure 1 shows the BJH pore size distribution of the calcined and acid-treated samples. For the calcined samples, the pore size distribution was broad and centered at a maximum pore diameter value of 25−30 nm, for the $n \geq 0.5$ samples. For the $n = 0.25$ sample, the maximum pore diameter was around 15 nm. After acid treatment, the development of narrower pores and an increase in pore volume were observed for the $n = 1$ and $n = 0.75$ samples (Figure 1 and Table 1). This could be explained by the dissolution of the amorphous manganese species, unveiling the narrow mesoporous distribution present in the particles. For the $n \leq 0.5$ samples, no significant effect to the pore size distribution or pore volume was observed after the H_2SO_4 treatment.

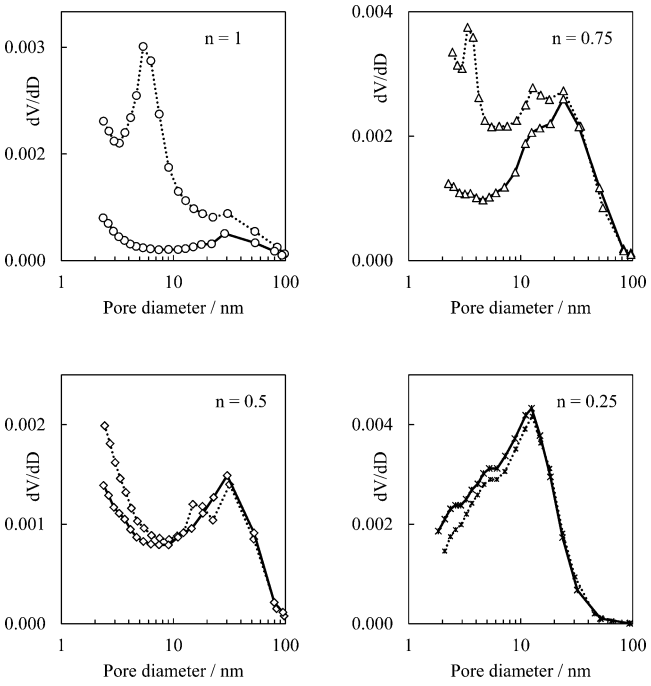

Figure 1. BJH pore size distribution obtained on the $(n)MnO_x-(1-n)CeO_2$ samples calcined (straight line) and acid-treated (dotted line).

In order to investigate the effect of the acid treatment on the sample morphology, TEM analysis was carried out for the $n = 1$ sample, in which the acid treatment strongly modifies the surface area and pore size distribution. The calcined sample consists of sphere-like nanoparticles, as shown in Figure 2a. The diffraction plane of the MnO_x sample can also be observed by HRTEM (Figure 2a inset); for the calcined sample, the (2 0 0) orientation corresponding to Mn_5O_8 was identified (d_{200} = 0.4894 nm). After the acid treatment, the presence of smaller particles together with larger sphere-like nanoparticles is detected (Figure 2b). Small particles (size around 10 nm) surround larger particles (~100 nm), supporting the explanation given above, where dissolution of amorphous manganese species located between the particles occurs to unveil the porosity of the larger particles.

Higher magnification images of the sample treated with sulfuric acid are shown in Figure 2c; the acid treatment strongly modified the size and shape of the particles from sphere-like nanoparticles of 60 nm to small plate-like particles of 10 nm. The particle size distribution is strongly modified after acid treatment (Figure 2d). Indeed for the calcined and acid-treated samples, the particle size distribution is centered at around 70 and 10 nm, respectively.

3.1.2. Redox Properties. Figure 3a shows the H_2-TPR profiles of the calcined MnO_x-CeO_2 samples. The H_2-TPR profile of pure ceria reveals small peaks between 200 and 400 °C, which could be assigned to the reduction of easily reducible surface cerium.[32] For the $n = 0.25$ and $n = 0.5$ samples, the reduction peaks appear over a rather broad temperature range (100−500 °C) with overlapping peaks characterized by two apparent maxima at 240 and 340 °C. Several authors have reported a similar reduction behavior in MnO_x-CeO_2.[28,33,34] The reduction process at lower temperatures results in the formation of a Mn−Ce−O solid solution in which the mobility of oxygen species is greatly enhanced. For the $n = 0.75$ and $n = 1$ samples, two main reduction peaks with maxima at around 310 and 460 °C were observed. The low-temperature reduction peak could be ascribed to the reduction of Mn_5O_8 and Mn_2O_3 into Mn_3O_4, whereas the high-temperature reduction peak could be assigned to a further reduction of Mn_3O_4 into MnO.[13]

Figure 3b shows the H_2-TPR profiles of the acid-treated MnO_x-CeO_2 samples. The reduction profile at low temperature for the $n = 0.25$ and $n = 0.5$ samples disappeared, and a reduction peak at around 540 °C appeared. The presence of this peak in the TPR profile of all Ce containing samples suggested the formation of $Ce(SO_4)_2$ through the acid treatment and reduction of sulfate species by H_2 most probably occurring in this temperature range. A strong impact of acid treatment is observed for the $n = 1$ sample. In comparison with the calcined one, the reduction took place at a much lower temperature. A higher contribution for the first reduction peak toward the total reduction profile is also clearly seen, corresponding to manganese ions in higher oxidation states (Mn_5O_8 instead of Mn_3O_4).

Table 2 summarizes the total H_2 consumption values calculated from the H_2-TPR profiles. For the calcined and acid-treated samples, the total H_2 consumption increased with

DOI: 10.1021/cs501879j
ACS Catal. 2015, 5, 2260−2269

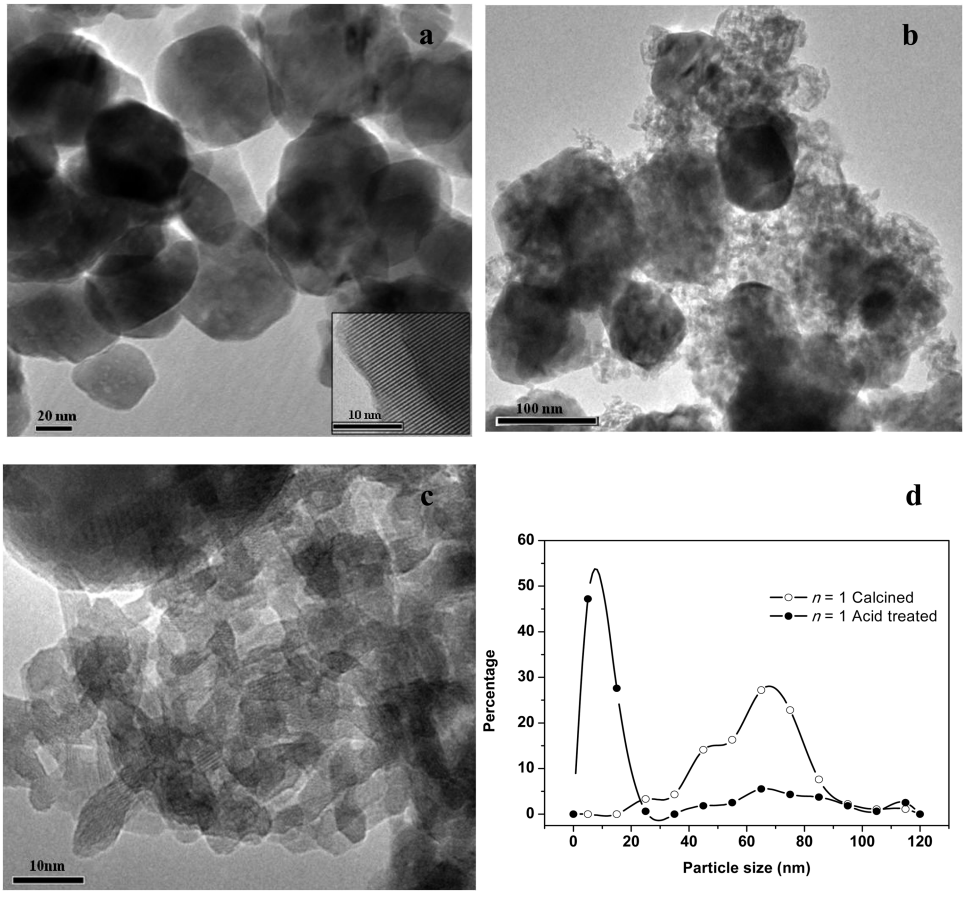

Figure 2. (a) TEM images of calcined n = 1 sample, (b) TEM images of acid-treated n = 1 sample, (c) HRTEM of acid-treated sample, and (d) particle size distribution of the calcined and acid-treated n = 1 sample from TEM images.

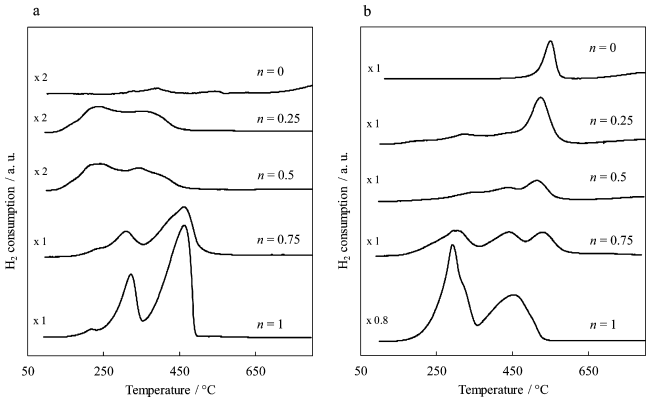

Figure 3. H_2-TPR profiles of the $(n)MnO_x-(1-n)CeO_2$ samples: (a) calcined and (b) acid-treated.

Table 2. Quantitative Results from H_2-TPR for the $(n)MnO_x-(1-n)CeO_2$ Samples

	consumed H_2 (mmol·g^{-1})	
sample code (n)	calcined	acid-treated
1	6.2	8.6
0.75	3.4	3.9
0.5	2.4	2.8
0.25	2.1	2.0
0	0.2	0.9

the increase of Mn content in the samples. The acid treatment mainly affected the pure manganese (n = 1) and pure cerium (n = 0) samples for which a 39% and 350% increase in H_2 consumption is observed. For the n = 1 sample, the Mn average oxidation number increased from 3 (calcined sample) to 3.4 (acid-treated sample). This result can be correlated to the presence of a Mn_5O_8 phase observed by XRD after the acid treatment. For the n = 0 sample, the increase in H_2 consumption could be explained by the reduction of sulfate species at 540 °C.

3.1.3. XPS Analyses. The Ce 3d XP spectra (not shown) were first investigated in order to ascertain the oxidation state of cerium. In the Ce $3d_{3/2,5/2}$ spectra, the presence of the six peaks (u, u″, u‴, v, v″, and v‴) and that of the satellite peak located at 916.7 eV (u‴) in all Ce samples (calcined and acid-treated) are observed. These peaks are characteristic of the presence of Ce^{4+} ions.[35] Chemical activation did not affect the oxidation state of cerium.

Owing to the presence of unpaired electrons in Mn(II), Mn(III), Mn(IV) species, the electronic spectrum of Mn 2p exhibits multiplet structures, leading to difficulties in identifying the chemical state of Mn. The Mn 2p XPS signal (not shown) in all samples is centered at a BE of around 642 eV. For n = 0.75 and n = 1, considering both calcined and acid-treated samples, a shoulder at low BE (639.8 eV) is observed. This additional contribution might correspond to the divalent Mn ions in Mn_5O_8 and/or Mn_3O_4, previously identified by XRD analysis.

DOI: 10.1021/cs501879j
ACS Catal. 2015, 5, 2260−2269

The XPS spectra of the core levels of Mn 3s were used to estimate the average oxidation state (AOS) of Mn. The Mn AOS has been calculated using the linear relationship between the Mn 3s multiplet splitting energy (ΔE) and the AOS of Mn.[36] The values of Mn AOS obtained from the XPS study for the n = 1 samples are in agreement with those obtained from H_2-TPR analyses. The variation in Mn AOS as a function of cerium content in the samples is reported in Figure S3. For calcined samples, the Mn AOS remained almost constant (around 2.9) with increasing cerium content in the sample. For the acid-treated samples, the Mn AOS was strongly enhanced for the n = 0.75 (3.6) and n = 1 (3.9) samples. This result suggests that the sulfuric acid reacts with the MnO_x phases present in the calcined n = 0.75 and n = 1 samples. The formation of a Mn−Ce−O solid solution resulting from the dispersion of manganese species in the lattice inhibits the oxidation of manganese species once the acid treatment is carried out.

O 1s XP spectra of the calcined samples are shown in Figure 4. The main line between 530 and 529.4 eV is attributed to the

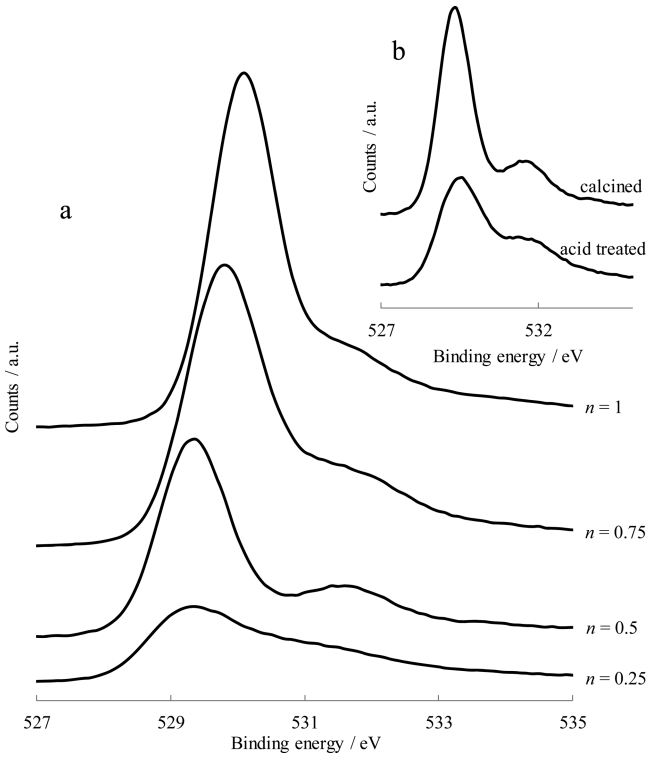

Figure 4. O 1s XP spectra of the (a) calcined $(n)MnO_x-(1-n)CeO_2$ samples, (b) calcined and acid-treated n = 0.5 samples.

lattice oxygen (O_L) in MnO_x-CeO_2 samples. O_L BE decreased with decreasing Mn content in the sample, owing to the change in the O^{2-} species environment. The shoulder on the high binding energy side is due to the presence of chemisorbed oxygen (O_2^-, O^-, OH^-). After chemical activation, the shoulder becomes relatively more pronounced (Figure 4b), and this can be explained by the presence of oxygen from sulfate species, as sulfur has been observed in acid-treated samples in the form of sulfates (S 2p BE at 169 eV).[37]

Surface composition values from XPS data are gathered in Table 3. The Mn/(Mn + Ce) ratio values remain identical after chemical activation, confirming the preservation of the solid solution. A proportional increase in sulfur with increasing Ce

Table 3. Surface Atomic Composition from XPS Analyses

	Mn/(Mn + Ce)		S/(Mn + Ce)
sample code (n)	calcined	acid-treated	acid-treated
1	1.00	1.00	0.03
0.75	0.60	0.59	0.10
0.5	0.25	0.27	0.25
0.25	0.18	0.18	0.42

concentration is observed and can be explained by the interaction between the sulfate and cerium species.

3.2. Reactivity. *3.2.1. Catalytic Test.* Figure S4 shows the light-off curves obtained for the HCHO conversion as a function of temperature in the presence of the calcined (Figure S4a) and acid-treated catalysts (Figure S4b). For the calcined samples, the order of activity found on the basis of T_{50} (temperature at 50% of HCHO conversion) values is the following: n = 0.25 > n = 0.75 > n = 0.50 > n = 1 > n = 0. For acid-treated samples, a different behavior is observed because T_{50} decreases with increasing Mn loading: n = 1 > n = 0.75 > n = 0.50 > n = 0.25 > n = 0. Irrespective of the reaction temperature, for all Mn-containing samples, H_2O and CO_2 are the only products observed, whereas in the presence of pure ceria, CO (selectivity of 30% at 100% conversion), CH_3-OH and HCOOH (not quantified) are also detected.

Figure 5 shows the HCHO conversion at 100 °C as a function of Mn/(Mn+Ce) molar surface ratio in MnO_x-CeO_2

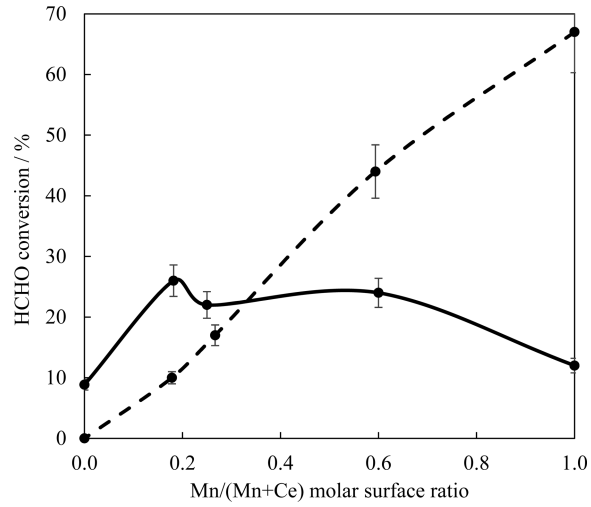

Figure 5. HCHO conversion (%) evaluated at 100 °C as a function of Mn/(Mn + Ce) molar surface ratio in calcined (straight line) and acid-treated (dotted line) MnO_x-CeO_2 catalysts.

catalysts. The chemical composition of the calcined and acid-treated catalysts has a significant impact on the formaldehyde conversion. In the presence of calcined mixed oxides, the formaldehyde conversion is much better than those of single oxides. Tang et al.[9,38] already showed evidence of the enhancement in the formaldehyde conversion for the Mn/Ce mixed oxides compared to pure MnO_x and CeO_2. For the calcined mixed oxides, HCHO conversion activity is ranked as follows: n = 0.25 > n = 0.75 ~ n = 0.5. This result can be related to the specific surface, which is largest for the n = 0.25 calcined sample.

In the presence of acid-treated catalysts, the HCHO conversion increases monotonically with the Mn content in

DOI: 10.1021/cs501879j
ACS Catal. 2015, 5, 2260−2269

the sample (Figure 5). In comparison with calcined samples, improvement in catalytic performances is observed for the n = 0.75 and n = 1 acid-treated samples. This can be related to the increase of specific surface area and to the promotion of redox properties at lower temperature due to the presence of manganese species in a higher oxidation state. For Ce-rich acid-treated samples (n = 0, 0.25, and 0.5), the HCHO conversion decreases in comparison with the parent calcined samples. Because no change in specific surface area has been registered for these samples after the acid treatment, the adverse effect could be explained by surface poisoning by sulfate species such as $Ce(SO_4)_2$, previously shown by XPS and H_2-TPR analyses. This phase is probably catalytically inactive toward HCHO oxidation.

For a better comparison of activity among catalysts with different surface areas, the reaction rates of HCHO oxidation were calculated per unit of surface area at 100 °C. The evolution observed as a function of Mn/(Mn + Ce) molar surface ratio is plotted in Figure 6. The synergistic mechanism

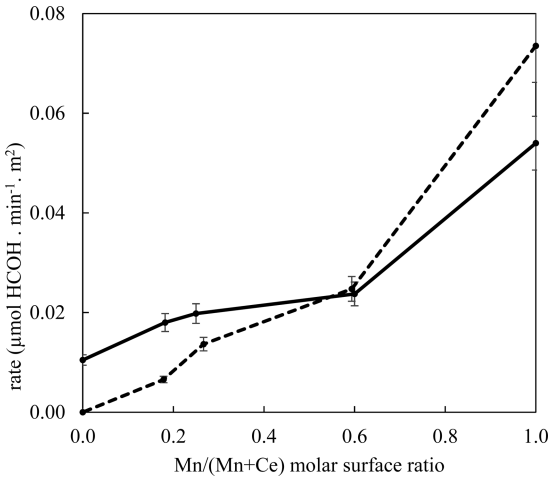

Figure 6. Intrinsic reaction rates of HCHO oxidation determined at 100 °C as a function of Mn/(Mn+Ce) molar surface ratio in calcined (straight line) and acid-treated (dotted line) MnO_x–CeO_2 catalysts.

in which the interaction between manganese and cerium oxides improves the oxygen transfer from molecular oxygen toward active sites of MnO_2 through an oxygen reservoir in CeO_2 has been proposed in different catalytic reactions.[39,40] However, in this case, the intrinsic reaction rate monotonically increases with the Mn content in the solid, showing that (i) Mn^{n+} species are more active that Ce^{4+} species in HCHO oxidation and (ii) a synergistic effect between the Mn and Ce oxides in the MnO_x–CeO_2 does not occur. The promoting effect in HCHO conversion (Figure 5) observed for the calcined mixed oxides (n = 0.25, 0.5, and 0.75) is thus mainly due to the increase in surface area. The intrinsic reaction rate is affected after acid treatment for n = 0, n = 0.25, and n = 0.5 catalysts, showing the adverse effect of sulfates in HCHO oxidation. A very high increase in intrinsic reaction rate is observed for the acid-treated pure manganese oxide. This result underlines the significance of the (i) Mn $(AOS)_{XPS}$ increase (from 2.9 to 3.85 after chemical activation, Figure S3) and (ii) improvement in redox properties (Figure 3b) for low-temperature HCHO oxidation.

In order to get more insight into the HCHO interaction with the catalyst surface, different surface reaction experiments have been performed. The acid-treated pure manganese oxide sample was selected to investigate the adsorption and transformation of formaldehyde upon heating under inert gas (argon). Additionally, HCHO temperature-programmed desorption, in situ XPS, and FTIR studies of samples previously exposed to formaldehyde have been performed.

3.2.2. Formaldehyde Adsorption and Surface Reaction Experiments. 3.2.2.1. HCHO Temperature-Programmed Desorption. Figure 7 shows the desorption profiles of different

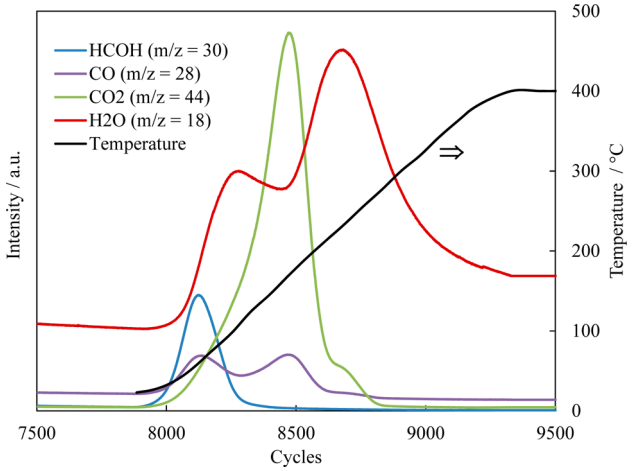

Figure 7. HCHO temperature-programmed desorption on the acid-treated MnO_x sample.

product species for the n = 1 acid-treated sample after HCHO adsorption. HCHO desorption between 50 and 100 °C can be observed with a maximum value around 50 °C. Carbon dioxide desorption also takes place in a single broad peak, between 50 and 250 °C, with a maximum at 180 °C. Carbon monoxide is found to desorb in two stages between 30 and 200 °C—the first one occurred in the temperature range of HCHO desorption, and the second one took place together with CO_2 desorption. Water is also found to desorb from the surface in two broad peaks with maxima at 100 and 230 °C.

The water production in the low-temperature range can be related to the production of OH species on the surface, as a result of the formation of formate species with the participation of oxygen ("O") from the manganese oxide (step (1)). Indeed, the formation of adsorbed formate species ($HCOO_{(ad)}$) is often proposed as an intermediate in the oxidation of formaldehyde.[41,42]

$$HCHO_{(g)} + 2\text{“O”} \rightarrow HCOO_{(ad)} + OH_{(ad)} \quad (1)$$

$$2OH_{(ad)} \rightarrow H_2O_{(g)} + \text{“O”} \quad (2)$$

At higher temperature, the formation of oxidation products (CO or CO_2) could result in the oxidation of formate species with the participation of oxygen from the MnO_x solid (steps (3) and (4)) and the desorption of water in the reaction between $OH_{(ad)}$ and $H_{(ad)}$ (step (5)):

$$HCOO_{(ad)} \rightarrow CO_{(g)} + OH_{(ad)} \quad (3)$$

$$HCOO_{(ad)} \rightarrow CO_{2(g)} + H_{(ad)} \quad (4)$$

$$OH_{(ad)} + H_{(ad)} \rightarrow H_2O_{(g)} \quad (5)$$

The HCHO-TPD experiment strongly suggests the participation of oxygen from manganese oxide in the reaction, giving

DOI: 10.1021/cs501879j
ACS Catal. 2015, 5, 2260–2269

rise to the formation of surface oxidation products such as formate species. In order to gain more understanding, in situ Fourier transform infrared spectroscopy between RT and 200 °C was carried out on the same sample previously exposed to formaldehyde.

3.2.2.2. In Situ Fourier Transform Infrared Spectroscopy of the Formaldehyde-Exposed MnO_x. IR spectra obtained at different temperatures are shown in Figure S5. Four intense bands related to formate species adsorbed on the catalyst surface[41] at 2864 (ν_{CH}), 1573 (asym ν_{OCO}), 1371 (δ_{CH}), and 1355 cm^{-1} (sym ν_{OCO}) are observed together with a large band near 3300 cm^{-1} associated with hydroxyl groups in interaction with adsorbed formate species. This result is in perfect agreement with step (1). These species are stable up to 215 °C. However, the relative intensity of IR bands at 1371 and 1355 cm^{-1} changed during the temperature-programmed surface reaction, which suggested the presence of two different formate species. In order to appreciate the evolution of the formate species upon heating, the difference spectra have been plotted (Figure 8). The bands corresponding to formate species

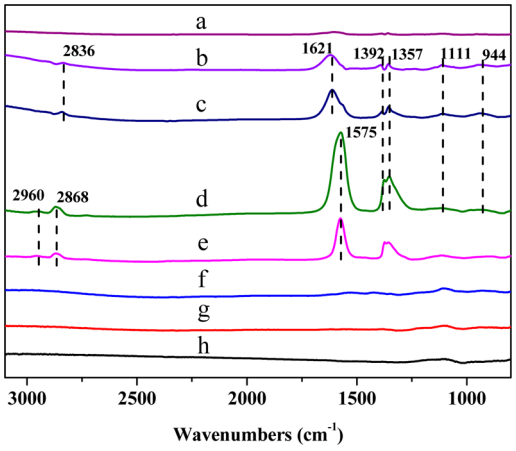

Figure 8. Difference between successive IR spectra recorded during the temperature-programmed surface reaction on the acid-treated MnO_x sample (a: 39−21 °C, b: 78−39 °C, c: 121−78 °C, d: 166−121 °C, e: 215−166 °C, f: 266−215 °C, g: 319−266 °C, h: 373−319 °C).

can be clearly seen between 20 and 215 °C. Moreover, the principal bands related to $\nu(OCO)_{as}$ are shifted toward lower wavenumbers from 1621 to 1576 cm^{-1}. The relative intensity of the bands present between 1300 and 1400 cm^{-1} also evolved. Formate can be adsorbed in two forms on the surface (i.e., monodentate and bidentate-bridging).[42,43] The frequency separation between $\nu(OCO)_{as}$ and $\nu(OCO)_s$ is employed to distinguish these two forms.[44] The frequency separation at 78 °C was around 264 cm^{-1}, whereas at 215 °C, the frequency separation was 220 cm^{-1}. When the frequency separation is higher than 250 cm^{-1}, the monodentate species prevail over the bidentate-bridging formate species.[41] This result suggests that at low temperature (40−120 °C), the formate species are bound to the surface in a monodentate configuration, and as the sample was heated, the bidentate-bridging formate configuration predominates. A similar trend was underlined during the interaction of formic acid with amorphous manganese oxide.[43]This evolution is in agreement with the previous HCHO temperature-programmed desorption study. On the one hand, desorption of HCHO was mainly observed between 27 and 100 °C (Figure 7) when monodentate formate species adsorbed at the surface disappeared. On the other hand, total oxidation of HCHO to CO_2 (Figure 7) was obtained between 100 and 250 °C, underlining the specific reactivity of bidentate-bridging formate species on the acid-treated MnO_x catalyst.

3.2.2.3. In Situ XPS Studies of the Formaldehyde-Exposed MnO_x. The C 1s signal evolution for the samples heated at different temperatures is shown in Figure 9. The photopeak at

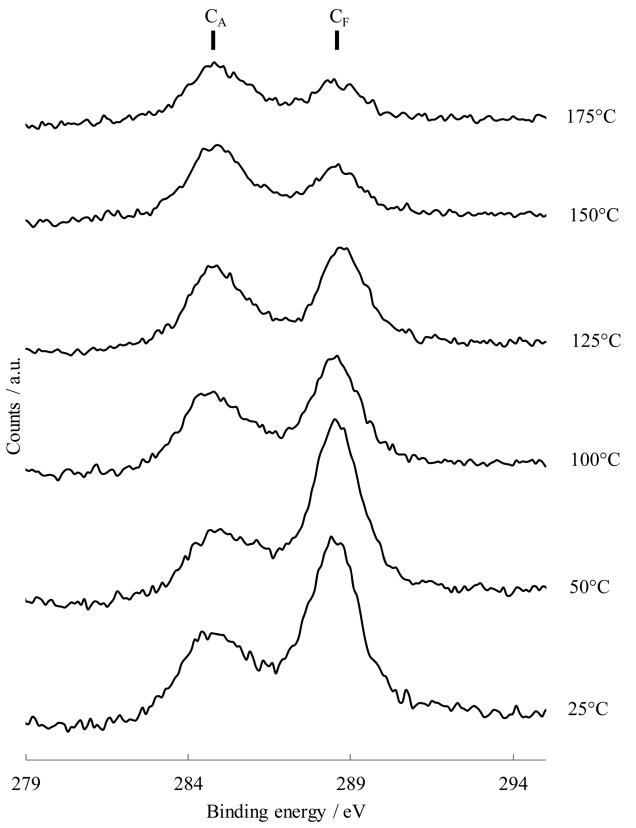

Figure 9. C 1s XP spectra evolution of the acid-treated MnO_x sample after HCHO adsorption and heating under Ar.

lower BE (284.5 eV) is assigned to adventitious carbon (C_A). The intensity of the C_A photopeak remains constant throughout heating. The photopeak at 288.5 eV is attributed to the presence of formate and/or formaldehyde (C_F) species. Indeed the C 1s BE of adsorbed formaldehyde on the TiO_2 (110) surface was determined to be 288.5 eV.[45] C 1s BE should be of the same magnitude for both formate and formaldehyde species, assuming the molecules are bonded end-on through the oxygen atom. Between 50 and 100 °C, a strong decrease in the intensity of the C_F photopeak with increasing temperature is observed (Figure 9). This can be explained by the formaldehyde and/or monodendate formate species desorption in this temperature range, observed by HCHO TPD and in situ FTIR. At higher temperature, the contribution of the C_F photopeak to the C 1s signal continues to decrease, and at the end, the C_F photopeak is less intense than the C_A photopeak. The formate species oxidation into gaseous CO and/or CO_2 (steps (3) and (4)) matches well with this observation in the temperature range 125−175 °C.

Based on the previous XPS study, the main contribution to the O 1s signal (Figure S6) comes from the lattice oxygen (O_L) at around 530 eV. In comparison with O 1s XP spectra of

DOI: 10.1021/cs501879j
ACS Catal. 2015, 5, 2260−2269

MnO_x without preadsorbed formaldehyde (Figure 4), the higher binding energy shoulder appearing at 532 eV (O_F) is much more pronounced after formaldehyde adsorption. This can be related to the presence of formate and formaldehyde species. The shoulder (O_F) becomes less pronounced with the increase in treatment temperature, in accordance with the formaldehyde desorption and formate oxidation.

The evolution of Mn AOS during the study is shown in Figure S7. After HCHO adsorption at RT, the Mn AOS is decreased from 3.9 (Figure S3) to 3.6 (Figure S7). This correlates perfectly to the oxidation of formaldehyde into formate species (step (1)) with the probable participation of lattice oxygen leading to Mn reduction. The Mn AOS evolution is in good agreement with formaldehyde and/or formate desorption without significant Mn AOS change from RT to 75 °C and with the formate oxidation with a decrease in Mn AOS from 100 to 175 °C (steps (3) and (4)).

4. CONCLUSION

In summary, acid treatment was conducted on MnO_x−CeO_2 mixed oxides synthesized by surfactant-assisted wet-chemistry. The substitution of Ce^{4+} by Mn species in the fluorite structure to form a solid solution was demonstrated in calcined and acid-treated samples with a Mn solubility limit of 50% in the fluorite structure. Textural and redox properties were found to be strongly altered by acid treatment (10M), especially when the Mn solubility limit was exceeded. Using H_2SO_4 as a reactive agent for the acid treatment, the specific surface area and pore volume were greatly increased owing to the dissolution of Mn^{2+} species present between the particles, unveiling the primary porosity and the oxidation of manganese species in the solid into a higher oxidation state. Among the calcined samples, mixed Mn/Ce oxides facilitated the complete oxidation of formaldehyde at lower temperature in comparison with pure CeO_2 and MnO_x oxides, owing to an increase in specific surface area and enhancement in the redox properties of the mixed metal oxides solid solutions. Moreover, a mechanistic study of formaldehyde reactivity on the best catalyst (chemically activated pure manganese oxide) for formaldehyde oxidation confirmed the participation of oxygen from manganese oxide through the formation of both monodentate and bidentate-bridging formate species, with different reactivity.

■ ASSOCIATED CONTENT

Supporting Information

The following file is available free of charge on the ACS Publications website at DOI: 10.1021/cs501879j.

Materials characterization (XRD, XPS and IR) data. HCHO catalytic conversion vs temperature (PDF)

■ AUTHOR INFORMATION

Corresponding Author

*E-mail: jean-francois.lamonier@univ-lille1.fr. Tel.: 33 3 20 33 77 33. Fax: 33 3 20 43 65 61.

Notes

The authors declare no competing financial interest.

■ ACKNOWLEDGMENTS

The authors are grateful to Olivier Gardoll (Lille1 University, France) for the H_2-TPR analyses. J.Q. thanks FUNDAYACUCHO (Caracas, Venezuela) and the French Embassy for the fellowship awarded. This research has been partially supported by the Nord-Pas de Calais Region in France through the Institute of Research in Industrial Environment (IRENI) project and by a French−Italian research project (PHC Galilee 2011 no. 25955PK). The TEM and XPS facilities in Lille (France) are supported by the "Conseil Regional du Nord-Pas de Calais" and the European Regional Development Fund (ERDF).

■ REFERENCES

(1) Salthamer, T.; Mentese, S.; Marutsky, R. *Chem. Rev.* **2010**, *110*, 2536−2572.
(2) Sekine, Y. *Atmos. Environ.* **2008**, *36*, 5543−5547.
(3) Quiroz, J.; Royer, S.; Bellat, J.-P.; Giraudon, J.-M.; Lamonier, J.-F. *ChemSusChem* **2013**, *6*, 578−592.
(4) Nie, L. H.; Yu, J. G.; Li, X. Y.; Liu, G.; Jaroniec, M. *Environ. Sci. Technol.* **2013**, *47*, 2777−2783.
(5) Zhang, C. B.; Liu, F. D.; Zhai, Y. P.; Ariga, H.; Yi, N.; Liu, Y. C.; Asakura, K.; Flytzani-Stephanopoulos, M.; He, H. *Angew. Chem., Int. Ed.* **2012**, *51*, 9628−9632.
(6) Nie, L. H.; Meng, A. Y.; Yu, J. G.; Jaroniec, M. *Sci. Rep.* **2013**, *3*, Articleno. 3215.
(7) Huang, H. B.; Leung, D. Y. C. *ACS Catal.* **2011**, *1*, 348−354.
(8) Zhang, C.; Li, Y.; Wang, Y.; He, H. *Environ. Sci. Technol.* **2014**, *48*, 5816−5822.
(9) Tang, X. F.; Chen, J. L.; Huang, X. M.; Xu, Y. D.; Shen, W. J. *Appl. Catal., B* **2008**, *81*, 115−121.
(10) An, N.; Wu, P.; Li, S.; Jia, M.; Zhang, W. *Appl. Surf. Sci.* **2013**, *285*, 805−809.
(11) Ma, C. Y.; Wang, D. H.; Xue, W. J.; Dou, B. J.; Wang, H. L.; Hao, Z. P. *Environ. Sci. Technol.* **2011**, *45*, 3628−3634.
(12) Zhang, C.; He, H. *Catal. Today.* **2007**, *126*, 345−350.
(13) Quiroz, J.; Giraudon, J.-M.; Lamonier, J.-F. *Catal. Today.* **2011**, *176*, 277−280.
(14) Liu, X.; Lu, J.; Qian, K.; Huang, W.; Luo, M. *J. Rare Earths.* **2009**, *27*, 418−424.
(15) Bai, L.; Wyrwalski, F.; Lamonier, J.-F.; Khodakov, A. Y.; Monflier, E.; Ponchel, A. *Appl. Catal., B* **2013**, *138*, 381−390.
(16) Chen, H.; He, J.; Zhang, C.; He, H. *J. Phys. Chem. C* **2007**, *111*, 18033−18038.
(17) Zhou, L.; Zhang, J.; He, J.; Hu, Y.; Tian, H. *Mater. Res. Bull.* **2011**, *46*, 1714−1722.
(18) Averlant, R.; Royer, S.; Giraudon, J.-M.; Bellat, J.-P.; Bezverkhyy, I.; Weber, G.; Lamonier, J.-F. *ChemCatChem.* **2014**, *6*, 152−161.
(19) Brenet, J.; Beley, M. *Electrochim. Acta* **1973**, *18*, 1003−1011.
(20) Askar, M.; Abbas, H. *J. Power Sources* **1994**, *51*, 319−330.
(21) Sinha, A.; Suzuki, K.; Takahara, M.; Azuma, H.; Nonaka, T.; Suzuki, N.; Takahashi, N. *J. Phys. Chem. C* **2008**, *112*, 16028−16035.
(22) Sinha, A.; Susuki, K.; Takahara, M.; Azuma, H.; Nonaka, T.; Fukumoto, K. *Angew. Chem., Int. Ed.* **2007**, *46*, 2891−2894.
(23) Imamura, S.; Shono, M.; Okamoto, N.; Hamada, A.; Ishida, S. *Appl. Catal., A* **1996**, *142*, 279−288.
(24) Tang, X.; Li, Y.; Huang, X.; Xu, Y.; Zhu, H.; Wang, J.; Shen, W. *Appl. Catal., B* **2006**, *62*, 265−273.
(25) Tian, Z.; Tong, W.; Wang, J.; Duan, N.; Krishnan, V.; Suib, S. *Science* **1997**, *276*, 926−930.
(26) Terribile, D.; Trovarelli, A.; De Leitenburg, C.; Dolcetti, G.; Llorca, J. *Chem. Mater.* **1997**, *9*, 2676−2678.
(27) Terribile, D.; Trovarelli, A.; Llorca, J.; De Leitenburg, C.; Dolcetti, G. *J. Catal.* **1998**, *178*, 299−308.
(28) Zou, Z.-Q.; Meng, M.; Zha, Y.-Q. *J. Phys. Chem. C* **2010**, *114*, 468−477.
(29) Monti, D. A. M.; Baiker, A. *J. Catal.* **1983**, *83*, 323−335.
(30) Machida, M.; Uto, M.; Kurogi, D.; Kijima, T. *Chem. Mater.* **2000**, *12*, 3158−3164.
(31) Um, M.; Miyake, M.; Hirato, T. In *Green Energy and Technology*; Yao, T., Ed.; Springer: Berlin, 2011; p 165.
(32) Laachir, A.; Perrichon, V.; Badri, A.; Lamotte, J.; Catherine, E.; Lavalley, J. C.; El Fallah, J.; Hilaire, L.; Le Normand, F.; Quéméré, E.;

DOI: 10.1021/cs501879j
ACS Catal. 2015, 5, 2260−2269

Sauvion, G. N.; Touret, O. *J. Chem. Soc. Faraday Trans.* **1991**, *87*, 1601−1609.
(33) Xingyi, W.; Qian, K.; Dao, L. *Appl. Catal., B* **2009**, *86*, 166−175.
(34) Chen, H.; Sayari, A.; Adnot, A.; Larachi, F. *Appl. Catal., B* **2001**, *32*, 195−204.
(35) Abi-aad, E.; Bechara, R.; Grimblot, J.; Aboukais, A. *Chem. Mater.* **1993**, *5*, 793−797.
(36) Gao, T.; Norby, P.; Krumeich, F.; Okamoto, H.; Nesper, R.; Fjellvåg, H. *J. Phys. Chem. C* **2010**, *114*, 922−928.
(37) Smirnov, M. Y.; Kalinkin, A. V.; Pashis, A. V.; Prosvirin, I. P.; Bukhtiyarov, V. I. *J. Phys. Chem. C* **2014**, *118*, 22120−22135.
(38) Tang, X.; Chen, J.; Li, Y.; Xu, Y.; Shen, W. *Chem. Eng. J.* **2006**, *118*, 119−125.
(39) Imamura, S.; Dol, A.; Ishido, S. *Ind. Eng. Chem. Prod. Res. Dev.* **1985**, *24*, 75−80.
(40) Qi, G.; Yang, R.; Chang, R. *Appl. Catal., B* **2004**, *51*, 93−106.
(41) Li, C.; Domen, K.; Maruya, K.; Onishi, T. *J. Catal.* **1990**, *125*, 445−455.
(42) Mao, C.; Vannice, A. *J. Catal.* **1995**, *154*, 230.
(43) Durand, J. P.; Senanayake, S. D.; Suib, S. L.; Mullins, D. R. *J. Phys. Chem. C* **2010**, *114*, 20000−20006.
(44) Busca, G.; Lorenzelli, V. *Mater. Chem.* **1982**, *7*, 89−126.
(45) Yuan, Q.; Wu, Z.; Jin, Y.; Xu, L.; Xion, F.; Ma, Y.; Huang, W. *J. Am. Chem. Soc.* **2013**, *135*, 5212−5219.

DOI: 10.1021/cs501879j
ACS Catal. 2015, 5, 2260−2269